Plasmonics (2025) 20:1551–1561
https://doi.org/10.1007/s11468-024-02386-2

RESEARCH

Dual-Core Photonic Crystal Fiber–Based Plasmonic Sensor for a Broad Range of Refractive Index Sensing

Umang Ramani[1] · Hemant Kumar[1] · Raj Kumar[2] · Bipin K. Singh[3] · Praveen C. Pandey[1]

Received: 3 April 2024 / Accepted: 6 June 2024 / Published online: 17 June 2024

Abstract

A dual-core photonic crystal fiber sensor using the surface plasmon resonance phenomenon has been demonstrated for a wide range of refractive index sensing. The proposed structure has a dual core with finite holes filled with air in the cladding section and four sides of C-shaped plasmonic layer arrangements. The gold metal layer is a plasmonic layer with TiO_2 dielectric layer. Simulation work is performed on COMSOL Multiphysics simulation software to determine the optimized structural parameters for efficient sensing performance. This sensor is compatible with analyte samples of refractive index (RI) range of 1.21–1.39. The value of maximum wavelength sensitivity is obtained 35,000 nm/RIU for an analyte sample RI 1.38–1.39 with an average sensitivity of 6368 nm/RIU and amplitude sensitivity is observed at 373 RIU^{-1} for the analyte sample of RI 1.38. The proposed PCF sensor reveals the wavelength resolution (R) of 2.85×10^{-6} RIU and the figure of merit (FOM) value of 259 RIU^{-1} for an analyte sample of RI 1.38. Due to the long range of analyte detection, this sensor has the potential to be developed as a sensor for biochemical and biomedical sensing applications as well as the detection of different organics containing fluorine.

Keywords Photonic Crystal Fiber · Refractive Index Sensor · Surface Plasmon Resonance · Sensitivity

Introduction

Surface plasmon resonance (SPR) is an emerging technology in the different sensing fields, which is a label-free and real-time technique [1]. Sensor with SPR technology has widespread applications in the area, such as bioimaging [2], environmental monitoring [3], and food monitoring [4]. This phenomenon is a collective oscillation of free electrons (e^-) at the metal and dielectric interface due to interlinkage with evanescent waves. In the earlier stage of SPR technology, a prism-based SPR sensing method was developed. The first method was named the Otto configuration, in which there is a prism and then an air gap followed by a metal layer arrangement. The light strikes on the prism base at an angle (θ) larger than the attenuated total reflection angle (θ_{ATR}) for excitation of surface plasmon wave (SPW). Improving this Otto configuration, Kretschmann used a conducting (metal) layer in contact with a prism in his setup and kept it in direct contact with the unknown analyte sample. Now, when (p-polarized) light falls at the prism metal interface at an angle ($\theta \geq \theta_{ATR}$), an evanescent wave is generated, which excites quanta known as surface plasmon moving parallel to the surface. When the power and frequency of the evanescent wave match the power and frequency of the surface plasmon wave (SPW), resonance occurs. This peculiar frequency is known as resonance frequency, and the phenomenon is called surface plasmon resonance [5]. Although this prism-based SPR setup improved sensitivity, it was a costly device with a bulky size with limited mechanism [6]. So, we need to find an alternative to this arrangement, and conventional optical fibers were looked upon for this purpose. Conventional optical fibers have mechanical stability for sensing with low confinement losses. Still, there was an issue with removing the outer jacket of fiber chemically or physically to bring the core directly into contact with the sensing region, which makes it fragile. Also, optical fiber lacks tuning parameters, limiting its application in different fields [7].

✉ Praveen C. Pandey
pcpandey.app@iitbhu.ac.in

[1] Department of Physics, Indian Institute of Technology (BHU), Varanasi 221005, India

[2] Department of Applied Science and Humanities, Invertis University, Bareilly 243123, India

[3] ANTS Ceramics Private Limited, Mumbai 401208, India

Photonic crystal fibers (PCFs) have become an emerging option for conventional optical fiber due to their flexible shape, different tunable geometrical parameters, and minimum size. PCFs are a single-material fiber (usually fused silica) that have a solid core with finite air holes available in a cladding zone that makes a suitable condition of total internal reflection (TIR), and this kind of fiber is known as solid core photonic crystal fiber [8]. Results obtained from PCF structures are far better than conventional optical fiber regarding confinement loss and sensitivity [9]. Two kinds of sensing mechanisms are available to utilize PCF sensors.

The first sensing mechanism is an internal coating–based sensing mechanism in which a plasmonic nanolayer is polished around an air hole of the cladding and an analyte is filled inside this air hole [10, 11]. Some research papers have been reported using internal coating–based sensing mechanisms [12, 13]. Rifat et al. have announced an internal coating approach–based sensor having maximum wavelength sensitivity (WS) obtained 3000 nm/RIU for a sample of refractive index (RI) range 1.46–1.49, and a maximum resolution $R = 2.4 \times 10^{-5}$ RIU [10]. In this mechanism, cleaning the air hole every time to fill different analytes again is a challenging task in actual practice. Coating the air holes with plasmonic material with uniformity is also tricky. So, due to these imperfections seen in the first mechanism, we move forward to the second mechanism, which is known as the external coating sensing mechanism. The plasmonic layer is coated on the outermost portion of the PCF structure so that it can be directly touched with the analyte, which is needed to be sensed [14–16]. Paul et al. have worked on the external coating–based mechanism and earned maximum wavelength sensitivity (WS) of 11,700 nm/RIU for a sample RI range of 1.33–1.41 [17]. Based on the fabrication process, detection, and operating method, this mechanism is easier and more comfortable than the previous one, so we have used this external coating sensing mechanism for our research [18].

Our study has presented a photonic crystal fiber with dual core (DC-PCF). Our PCF sensor has focused on an extended range of RI 1.21 to 1.39 analytes, from lower analyte (RI) to higher analyte (RI). As mentioned above, we have chosen an external coating–based sensing mechanism because of its easy implementation and fabrication process. Gold is used as a plasmonic metal layer with a nanolayer of TiO_2 cemented between the gold layer and PCF. The whole simulation work of our proposed sensor is performed on COMSOL Multiphysics version 6.0, where several simulations are performed to find the best geometrical parameters like air hole size, pitch size, the width of gold material, and the thickness of TiO_2. Variations of confinement loss with the air hole, plasmonic (gold) layer width, and adhesive TiO_2 layer width are invigilated. This proposed structure has great potential in different fields, such as biomedical and biochemical, to detect low to high RIs.

Structural Design and Theoretical Model

The cross-section display of the proposed sensor structure is mentioned in Fig. 1. We have structured a semicircular dual-core-based PCF with a proper opening to create a channel for interaction of evanescent wave to SPP mode at metal–dielectric interface. We are dealing

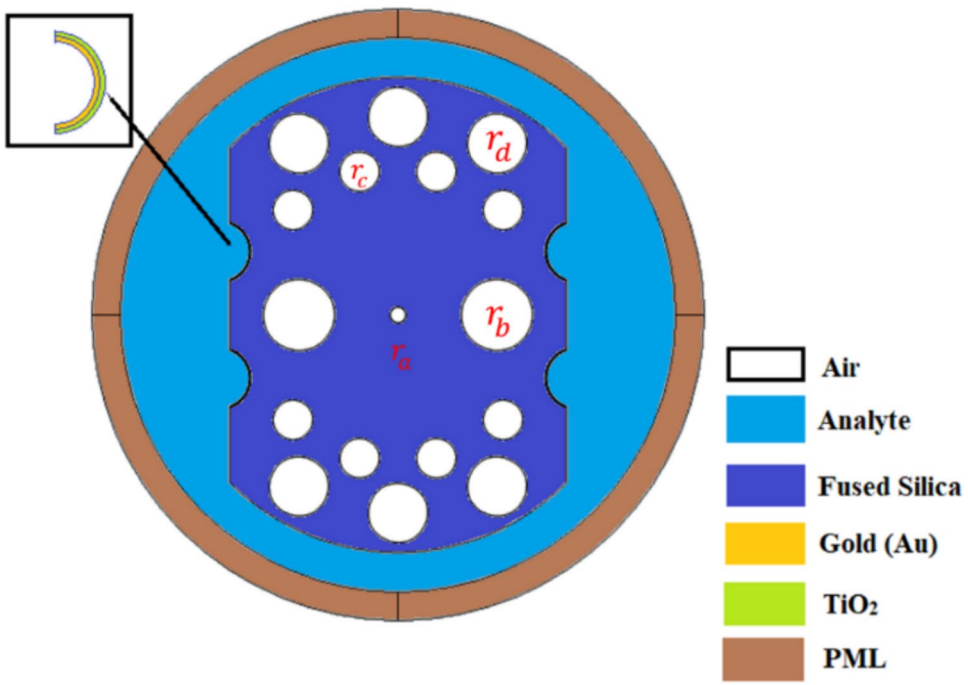

Fig. 1 A cross-section view of the proposed PCF sensor structure

with dual-core-based PCF with different sizes of air holes introduced in the cladding zone. There is a central hole between two cores of radius $r_a = 0.4\mu$m. Two holes are presented at both sides of the central hole with a radius $r_b = 1.8\mu$m, and other holes are presented in the cladding section with a radius $r_c = 1.0\mu$m and $r_d = 1.5\mu$m. The air holes with cores in structured dual-core PCF form a hexagonal lattice structure. We have considered co-ordinate values according to hexagonal lattice design in the simulation. Four sides of PCF are cut in a C-shape where laminations of the titanium dioxide (TiO_2) nanolayer and a plasmonic layer of gold (Au) are performed. In our proposed sensor structure, TiO_2 behaves as an adhesive layer for sensing performance enhancement. The width of the TiO_2 layer and plasmonic layer of gold (Au) is $t_{TiO_2} = 20$nm and $t_{Au} = 50$nm, respectively.

Fused silica is one of the best materials for PCF background, so we have chosen it as the background material for our proposed structure, and refractive index of fused silica is specified by following Sellmeier's equation [19]:

$$n^2(\lambda) = 1 + \frac{A_1\lambda^2}{\lambda^2 - B_1} + \frac{A_2\lambda^2}{\lambda^2 - B_2} + \frac{A_3\lambda^2}{\lambda^2 - B_3} \tag{1}$$

where $n(\lambda)$ is the refractive index (RI) of the background material (fused silica) depending on wavelength. Terms $A_{1,2,3}$ and $B_{1,2,3}$ are the Sellmeier constants, where $A_1 = 0.6961663$, $A_2 = 0.4079426$, and $A_3 = 0.8974794$, and $B_1 = 0.0684043\mu\text{m}^2$, $B_2 = 0.1162414\mu\text{m}^2$, and $B_3 = 9.896161\mu\text{m}^2$.

The Drude–Lorentz model has been adopted in our work to compute a frequency-based refractive index (RI) of plasmonic gold material, and its dispersive relation is given by the following equation [20]:

$$n^2_{Au}(\omega) = 5.9673 - \frac{\omega_D^2}{\omega \times (\omega + j\gamma_D)} - \frac{\Delta\epsilon \times \Omega_L^2}{(\omega^2 - \Omega_L^2) + j\omega\Gamma_L} \tag{2}$$

where n_{Au} is the index of refraction of gold (Au), and the parameter $\epsilon_\infty = 5.9673$ is called permittivity at a higher frequency and angular frequency expression $\omega = (\frac{2*pi*c}{\lambda})$, where c ($=3\times10^8$ m/s) and λ denote the light speed and wavelength, respectively. The term damping frequency and plasma frequency is symbolized by γ_D and ω_D with values $\gamma_D = 100.03$THz and $\omega_D = 13{,}280.14$ THz, respectively. The weighting factor is termed as $\Delta\epsilon = 1.09$. Terms denoting the strength of oscillator and spectral width of the Lorentz oscillator are $\Omega_L = 4084.51$ THz and $\Gamma_L = 658.85$ THz, respectively.

Titanium dioxide (TiO_2) is stacked between PCF cladding and the plasmonic layer to improve the analyte interaction, and RI of TiO_2 is calculated from the given below equation [20]:

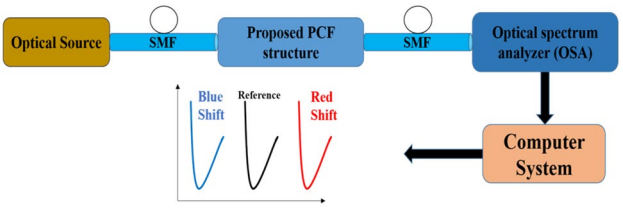

Fig. 2 The setup of the proposed PCF sensor

$$n^2_{TiO2} = A + \frac{B}{(\lambda^2 - C)} \tag{3}$$

Here, A, B, and C are constant and given by $A = 5.913$, $B = 2.441 \times 10^7$, and $C = 0.803 \times 10^7$ with wavelength (λ) regulated in a micrometer. To examine the characteristics of the proposed PCF structure, confinement loss is the crucial factor and it is given by [21]

$$\text{Confinement loss } (\alpha_{loss}) = 54.575 \times \frac{Im(n_{eff})}{\lambda_o} \times 10^4(\text{dB/cm}) \tag{4}$$

In the above formula, $Im(n_{eff})$ represents the imaginary part of the effective mode index and λ_o is the wavelength of the light incident. The complete setup of proper working of our PCF sensor using an optical light source, single-mode fiber, and the optical spectra analyzer (OSA) is depicted in Fig. 2. Numerical investigation and simulation of our PCF sensor structure are conducted using the finite element method (FEM), and simulation is performed in COMSOL Multiphysics version 6.0 [22]. In this method, the complete cross-section of the sensor is disunited into microscopic triangular elements called mesh elements. Using Maxwell's equation, coupled partial differential equations are solved to determine the longitudinal components

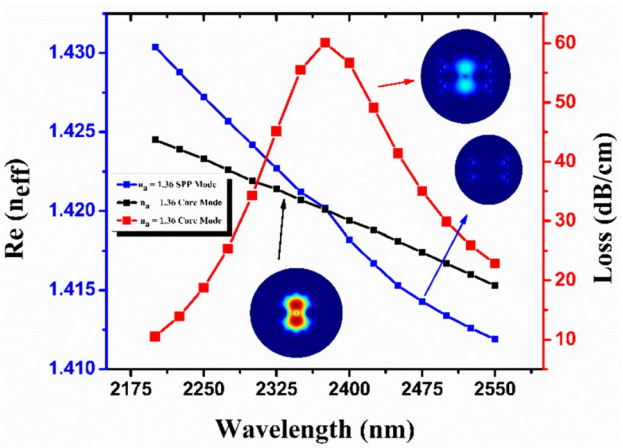

Fig. 3 Dispersion characteristics plot of core mode (black color) and SPP mode (blue color) for the analyte refractive index $n_a = 1.36$, with $r_a = 0.4\mu$m , $r_b = 1.8\mu$m , $r_c = 1.0\mu$m , $r_d = 1.5\mu$m , $t_{Au} = 50$nm , $t_{TiO_2} = 20$nm

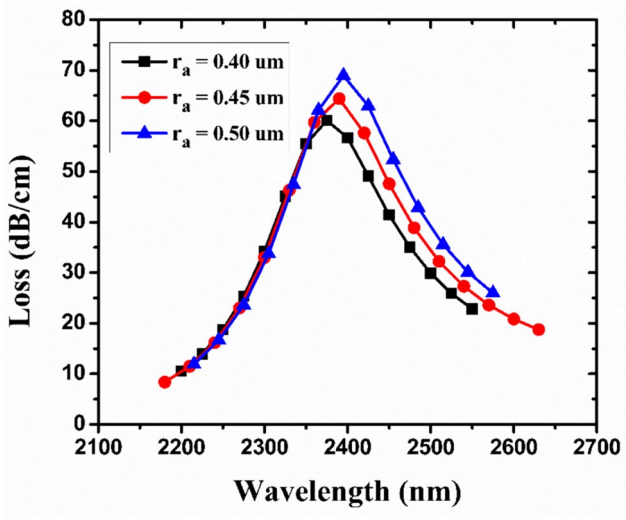

Fig. 4 Spectra of confinement loss for the central hole radius (r_a) alterations from 0.40 to 0.50 μm, with $r_b = 1.8\mu$m, $r_c = 1.0\mu$m , $r_d = 1.5\mu$m, $t_{Au} = 50$nm, $t_{TiO_2} = 20$nm

of the magnetic field and electric fields. To absorb the electromagnetic radiation at the outer surface, a perfect match layer (PML) is applied, and the width of this PML is kept around 10% of the fiber width [23].

Result and Discussion

In the simulation process, when (p-polarized) EM-wave starts to pass through the PCF core, the longitudinal part of the electric field reaches the plasmonic layer and generates an evanescent wave. This wave generates the core mode along with the SPP mode of PCF, and the dispersion characteristics of both modes are displayed in Fig. 3. It is understandable from the above figure that moving toward a red-shift in wavelength coupling strength between core mode and SPP mode becomes more assertive and reaches its peak value at a fixed wavelength termed as resonance wavelength. Then, it gets weakened after this peak point. At this resonance wavelength, the real part of the effective mode index of core mode and the real part of the effective mode index of SPP mode match, and the maximum amount of power is transported from core to SPP mode, named as confinement loss [21].

The next task is altering the geometrical parameters of the PCF sensor. We have performed simulations several times to determine the best geometrical parameter for our PCF sensor structure. Figure 4 disposes of the confinement loss with wavelength for the variations of the radius of the central hole (r_a) from 0.40 to 0.50 μm, and the confinement loss peaks have a red-shift because escalating air hole size coupling potency between core and SPP modes increases as a consequence of increment in Re (n_{eff}) of SPP mode [24].

Disturbing air hole size in the cladding segment $r_b = 1.8 - 2.6\mu$m and $r_c = 1.0 - 1.5\mu$m, the confinement loss spectrum has a downfall as depicted in Fig. 5. This happens because raising the size of these air holes makes it difficult for light to reach from the core to SPP modes and weakens the coupling between the two modes mentioned above [25]. Confinement loss spectra remain approximately stable with the extreme air hole radius (r_d) variations $r_d = 1.50 - 1.70\mu$m, as shown in Fig. 6.

The worthy change is observed with a variation of the gold (Au) layer and the sticky layer of TiO_2. Figure 7

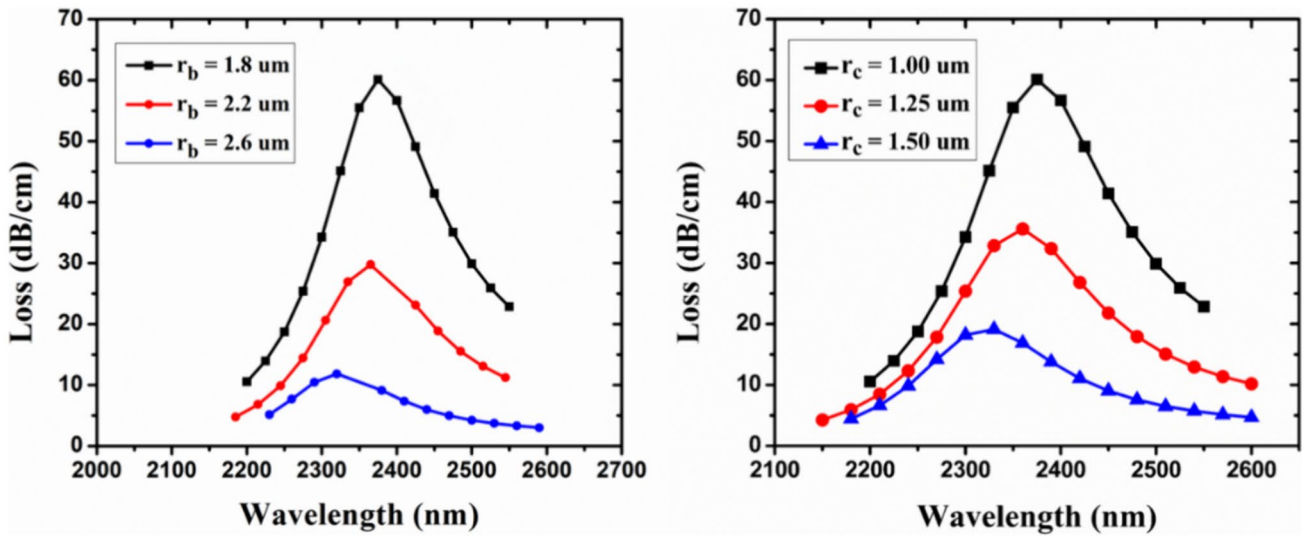

Fig. 5 Spectra of confinement loss for the variations of air hole radius **a** $r_b = (1.8 - 2.6)\mu$m and **b** $r_c = (1.0 - 1.5)\mu$m with $r_a = 0.4\mu$m , $r_d = 1.5\mu$m, $t_{Au} = 50$nm, $t_{TiO_2} = 20$nm

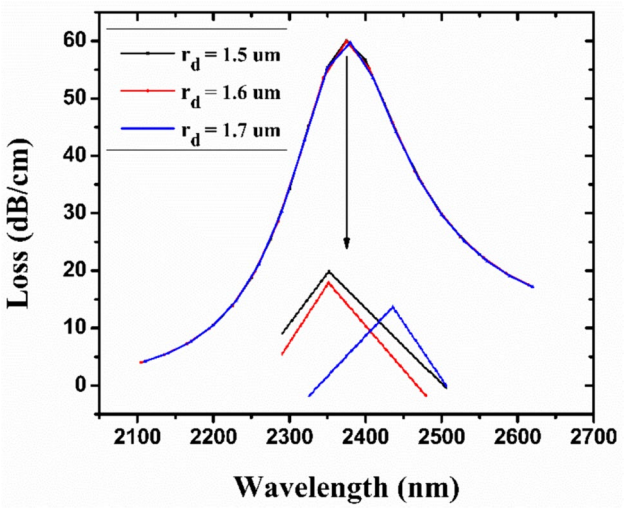

Fig. 6 Spectra of confinement loss for the variations of air hole radius $r_d = (1.5 - 1.7)\mu$m with $r_a = 0.4\mu$m, $r_b = 1.8\mu$m, $r_c = 1.0\mu$m, $t_{Au} = 50$nm, $t_{TiO_2} = 20$nm

indicates that the confinement loss reduces from 60.10 to 53.56 dB/cm for varying the width of the (Au) metal layer (t_{Au}) from 50 to 60 nm with a step size of 5 nm and the analyte RI (n_a) of 1.36. It happens for the reason that on escalating the width of the gold metal layer, high damping loss occurs, resulting in poor penetration of the electric field inside the analyte [26]. Remarkable beneficiation was made by a sticky nanolayer of TiO_2 [26]. Cementing this TiO_2 nanolayer (working as a catalyst) between PCF and plasmonic layer enhances the coupling strength between core and SPP modes. Hence, the confinement loss peak goes up from 60.10 to 80.11 dB/cm with increasing the thickness of TiO_2 from $t_{TiO_2} = 20 - 30$nm, as mentioned in Fig. 8.

The salient key parameter of the PCF sensor is known as wavelength sensitivity (WS), and it is given by [27]

$$Wavelength\ Sensitivity\left(S_\lambda\right) = {}^{\Delta\lambda_{peak}}/_{\Delta n_a}(nm/RIU) \tag{5}$$

Here, λ_{peak} is the resonance wavelength for a particular analyte RI. Our PCF structure is compatible with detecting a wide range of analytes RI $n_a = 1.21 - 1.39$. We observe that the confinement loss peak value enhances with increasing analyte refractive index because coupling becomes stronger between the core mode and SPP mode with an increasing refractive index of the analyte [28]. The maximum wavelength sensitivity (WS) value is 35,000 nm/RIU for analyte RI 1.38–1.39, and the average wavelength sensitivity is 6368 nm/RIU for analyte sample RI 1.21–1.39. The distribution of the confinement losses for the variations of the analyte sample RI (n_a) 1.21 to 1.39 is displayed in Fig. 9.

Another excellent tool to measure the term sensitivity of our sensor is amplitude sensitivity (S_A), which is homogenous to the wavelength sensitivity technique. It is a more cost-productive method than the wavelength sensitivity (WS) method because spectrum proficiency is unnecessary like the wavelength sensitivity (WS) method, and all measurement is performed at a defined wavelength. The amplitude sensitivity (S_A) is specified by the equation [29]

$$Amplitude\ sensitivity\left(S_A\right) = -\frac{1}{\alpha\left(\lambda, n_a\right)} \times \frac{\partial\alpha\left(\lambda, n_a\right)}{\partial n_a} RIU^{-1} \tag{6}$$

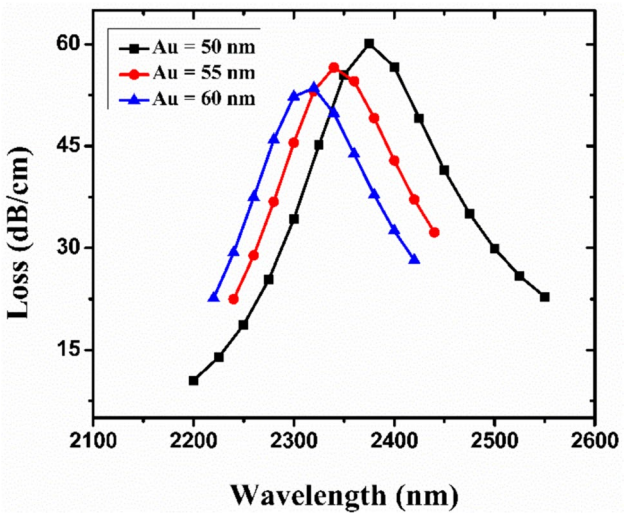

Fig. 7 Spectra of confinement loss with variable (Au) layer thickness with the analyte RI $n_a = 1.36$ with $r_a = 0.4\mu$m, $r_b = 1.8\mu$m , $r_c = 1.0\mu$m, $r_d = 1.5\mu$m, $t_{TiO_2} = 20$nm

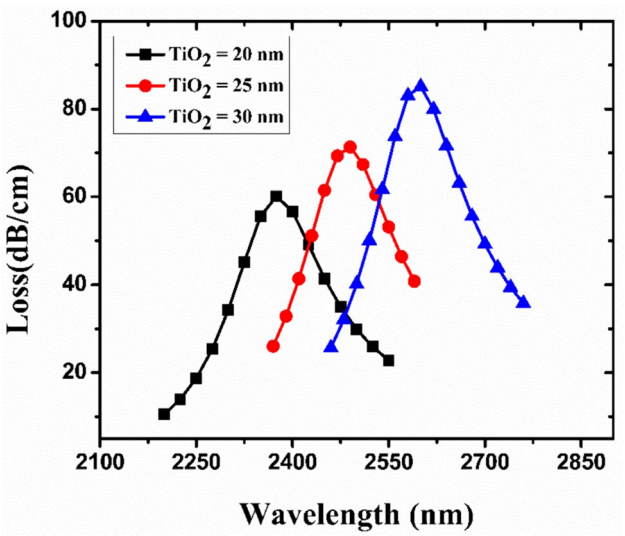

Fig. 8 Spectra of confinement loss for the variations of TiO_2 layer width with the analyte RI $n_a = 1.36$ with $r_a = 0.4\mu$m, $r_b = 1.8\mu$m, $r_c = 1.0\mu$m, $r_d = 1.5\mu$m, $t_{Au} = 50$nm

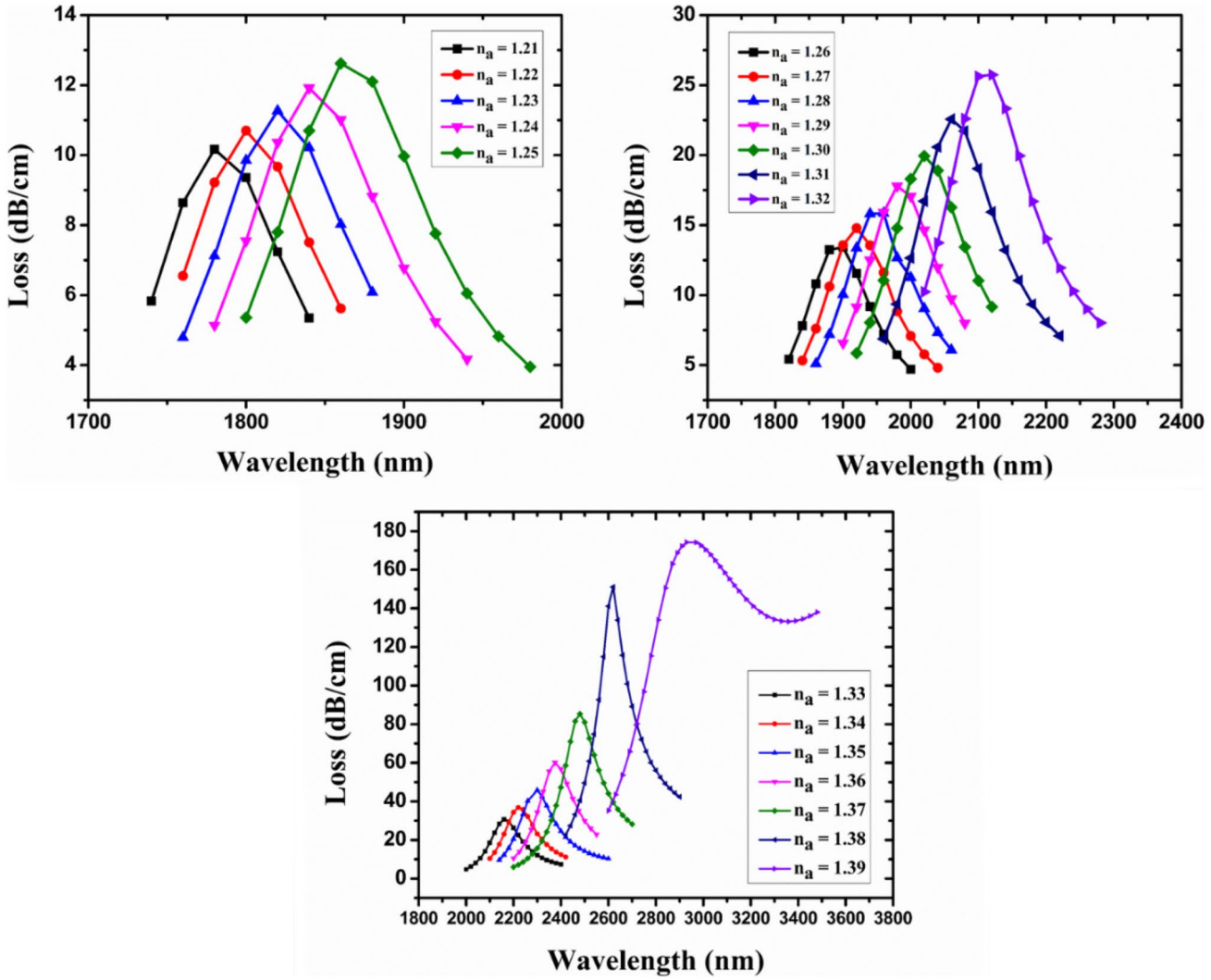

Fig. 9 Spectra of confinement loss for the variations of the analyte RI $n_a = 1.21$ to 1.39 with $r_a = 0.4\mu$m, $r_b = 1.8\mu$m, $r_c = 1.0\mu$m, $r_d = 1.5\mu$m, $t_{Au} = 50$nm, $t_{TiO_2} = 20$nm

where $\alpha(\lambda, n_a)$ is the net loss depth at a particular analyte RI and $\partial\alpha(\lambda, n_a)$ is the difference in confinement loss value for two nearby analytes' RIs at a particular wavelength (λ). The obtained value of amplitude sensitivity for our proposed sensor structure is 373 RIU^{-1} for the analyte sample RI $n_a = 1.38$, as depicted in Fig. 10.

A key feature to estimate the performance of the PCF sensor is its resolution, given by the following equation [30]:

$$Resolution(R) = \frac{\Delta\lambda_{min}}{S_\lambda} = \Delta n_a \times {}^{\Delta\lambda_{min}}/_{\Delta\lambda_{peak}} RIU \tag{7}$$

Considering the spectrometer resolution $\Delta\lambda_{min} = 0.1$nm, we observe the maximum resolution $R = 2.85 \times 10^{-6}$ RIU and the order of detection precision up to 10^{-6} means that the slightest change of order 10^{-6} can be detected for the analyte RI changes. A summary of the performance of PCF sensor work for effortless visualization is mentioned in Table 1. An extensive contrast of our proposed PCF sensor for the long-range analyte RI with other recently reported PCF RI sensor structures on the basis of their wavelength sensitivity are charted in Table 2.

Full-width half maxima (FWHM) is a crucial parameter used to compute our PCF sensor structure's figure of merit (FOM). A high value of FOM for a proposed PCF sensor structure indicates high performance and possible practical realization. The following equation gives the term FOM [31]:

$$FOM = \frac{Sensitivity(S_\lambda)}{FWHM}(RIU^{-1}) \tag{8}$$

We have analyzed the sensitivity and FWHM for a particular analyte RI. For analyte RI 1.38, the sensitivity value is 35,000 nm/RIU and FWHM is 135.31 nm; putting these

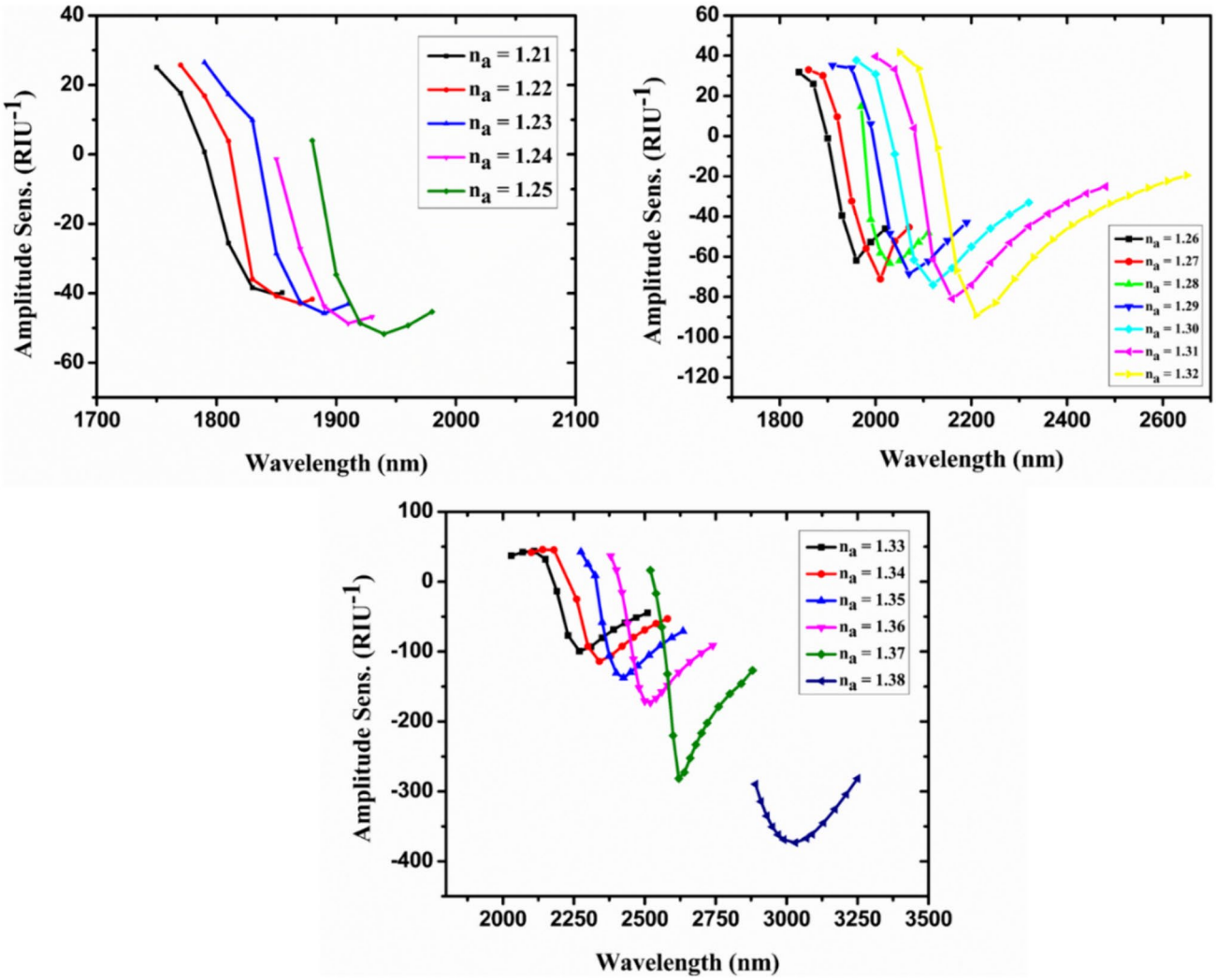

Fig. 10 The amplitude sensitivity variations for the analyte RI n_a= 1.21 to 1.39 with $r_a = 0.4\mu$m, $r_b = 1.8\mu$m, $r_c = 1.0\mu$m, $r_d = 1.5\mu$m, $t_{Au} = 50$nm, $t_{TiO_2} = 20$nm

values in Eq. (8), we get the FOM value of around 259 (RIU^{-1}) for our PCF sensor structure, as depicted in Fig. 11.

Since our proposed PCF sensor structure has an extensive analyte RI range $n_a = 1.21 - 1.39$ detection, it may be applied in different fields such as biomedical, biochemical, and other chemicals. Our sensor can be implemented to see the different types of organics which contain fluorine and have a low refractive index value ($n_a < 1.30$) such as 2,2,2-trifluoroethyl trifluoroacetate ($n_a = 1.2812$), trifluoroacetic acid ($n_a = 1.2850$), and 1,1,1,3,3,3-hexafluoro-2-propanol ($n_a = 1.275$) [30]. Nowadays, a significant issue in the medical field is detecting the cancer cell early for appropriate treatment. Several cancer cell tissues, such as cervical cancer, blood cancer, breast cancer, adrenal-gland cancer, and skin cancer, are reported for different types of cancer cells [37]. Their refractive index lies in the range of 1.36–1.39 , and our proposed sensor structure is designed for this analyte range detection. A pregnancy test based on the refractive index can also be performed using our proposed PCF structure. The refractive index of urine can be tested by putting a few drops of urine sample in the sensing area of our sensor. The general urine examination (GUE) test results show that all other factors remain the same such as glucose level, protein level, and uric acid. The detection of RI of the urine sample is most beneficial because the urine RI increases during pregnancy, and this increment is due to pregnancy hormone [38]. The next application of the proposed sensor structure in the row is alcohol detection by varying its concentration in water. The refractive index of water with 0% alcohol is 1.333. The refractive index of water mixed with alcohol varies from 1.3384, 1.3450, 1.3550, and so on for changing the concentration of alcohol in water, such as 10%, 20%, 30%, and so on, respectively [39]. So, this range can easily

Table 1 The performance of our PCF sensor for analyte RI range $n_a = 1.21 - 1.39$

Sample RI	**Wavelength (nm)**	**Res. peak shift (nm)**	**Wave. sens (nm/RIU)**	**Amp. sens (RIU^{-1})**	**Sensor resolution**	**Figure of merit (RIU^{-1})**
1.21	1780	20	2000	−40	5.00×10^{-5}	43
1.22	1800	20	2000	−43	5.00×10^{-5}	42
1.23	1820	20	2000	−46	5.00×10^{-5}	27
1.24	1840	20	2000	−49	5.00×10^{-5}	27
1.25	1860	40	4000	−52	2.50×10^{-5}	48
1.26	1900	20	2000	−62	5.00×10^{-5}	22
1.27	1920	40	4000	−71	2.50×10^{-5}	41
1.28	1960	20	2000	−63	5.00×10^{-5}	19
1.29	1980	40	4000	−69	2.50×10^{-5}	40
1.30	2020	40	4000	−74	2.50×10^{-5}	34
1.31	2060	60	6000	−81	1.67×10^{-5}	50
1.32	2120	40	4000	−89	2.50×10^{-5}	36
1.33	2160	60	6000	−100	1.67×10^{-5}	41
1.34	2220	80	8000	−114	1.25×10^{-5}	59
1.35	2300	75	7500	−138	1.33×10^{-5}	47
1.36	2375	105	10,500	−173	9.52×10^{-6}	65
1.37	2480	140	14,000	−281	7.14×10^{-6}	78
1.38	2620	350	35,000	−373	2.85×10^{-6}	259
1.39	2970	–	–	–	–	–

be identified with the help of the proposed PCF sensor because of its compatibility with this detection range.

Figure 12 represents the variations of the resonance wavelength with the analyte RI $n_a = 1.21 - 1.39$ and its third-order polynomial fitting. Correlation between the analyte RI and resonance wavelength (λ_{res}) for polynomial fitting is given by the equation $y = intercept + (B_1 \times x^1) + (B_2 \times x^2) + (B_3 \times x^3)$. In this equation, the y-axis represents the resonance wavelength (λ_{res}) and the x-axis represents the analyte RI. The values of intercept represented by B_1, B_2, and B_3 are mentioned in Fig. 12. It is clear from the figure that the statistical value of R^2 is 0.98293, which indicates the better fitting arrangement for our PCF sensor. PCF can be fabricated by several well-defined available technologies where a macroscopic preform of the desired shape is modulated and then drawn on microscopic scale fiber.

The available technologies for this task are extrusion [40], injection molding [41], sol–gel method [42], and stack-and-draw process [43]. Among these available technologies, the stack-and-draw method for PCF fabrication is the most promising, fast, clean, and cost-effective technology. This process has a few steps; the first step is fabrication, where capillaries of desired diameters are fabricated.

Table 2 The performance comparison of our PCF sensor with the recently reported PCF sensor

Reference	**Model structure**	**Analyte RI range**	**Wave. sens (nm/RIU)**	**Amp. sens (RIU^{-1})**	**Wave. resolution (RIU)**
[30]	D-shape PCF sensor	1.30–1.38	4250	NA	2.35×10^{-5}
[32]	Open channel PCF sensor	1.33–1.40	7000	594	1.43×10^{-5}
[33]	Broad-range PCF sensor	1.35–1.40	10,000	1115	2.00×10^{-5}
[34]	D-shape PCF sensor	1.33–1.39	11,500	230	8.7×10^{-6}
[35]	High perf. PCF sensor	1.29–1.34	13,800	2380	7.24×10^{-6}
[36]	Arc-shape PCF sensor	1.32–1.37	14,100	109	9.17×10^{-6}
Our work	Dual-core PCF sensor	1.21–1.39	35,000	373	2.85×10^{-6}

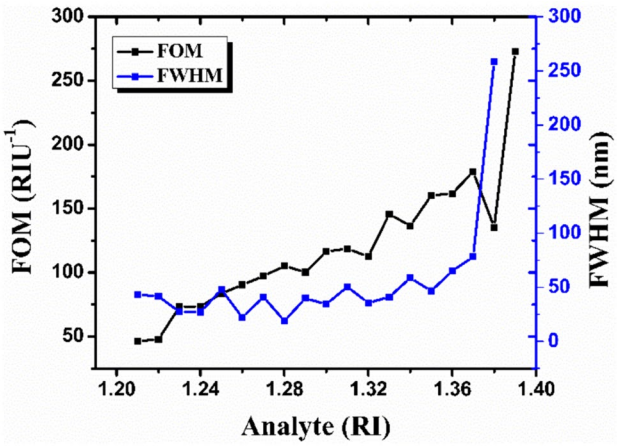

Fig. 11 The distributions of FOM and FWHM for analyte RI (n_a) variations from 1.21 to 1.39, with $r_a = 0.4\mu$m, $r_b = 1.8\mu$m, $r_c = 1.0\mu$m, $r_d = 1.5\mu$m, $t_{Au} = 50$nm, $t_{TiO_2} = 20$nm

Then, in the second step, they are stacked according to the required core cladding structure. After this process, the preform is extracted as microstructure rods and finally to a fiber in the last step. This process continues to repeat until we get the desired structure shape and parameters (diameter of fiber, air hole size, pitch) of the proposed PCF sensor. The subsequent work in sensor fabrication is to coat a plasmonic layer of gold and an adhesive layer of TiO_2. There are some approved technologies for the deposition of nanolayers, such as wet-chemistry deposition, thermal evaporation, and radiofrequency sputtering [44]. However, these methods undergo intense surface roughness due to a lack of uniformity of the nanolayer. That is why the chemical vapor deposition (CVD) method is better than the technologies mentioned above [45].

Fig. 12 Variation of resonance wavelength and polynomial fit with the analyte RI changes

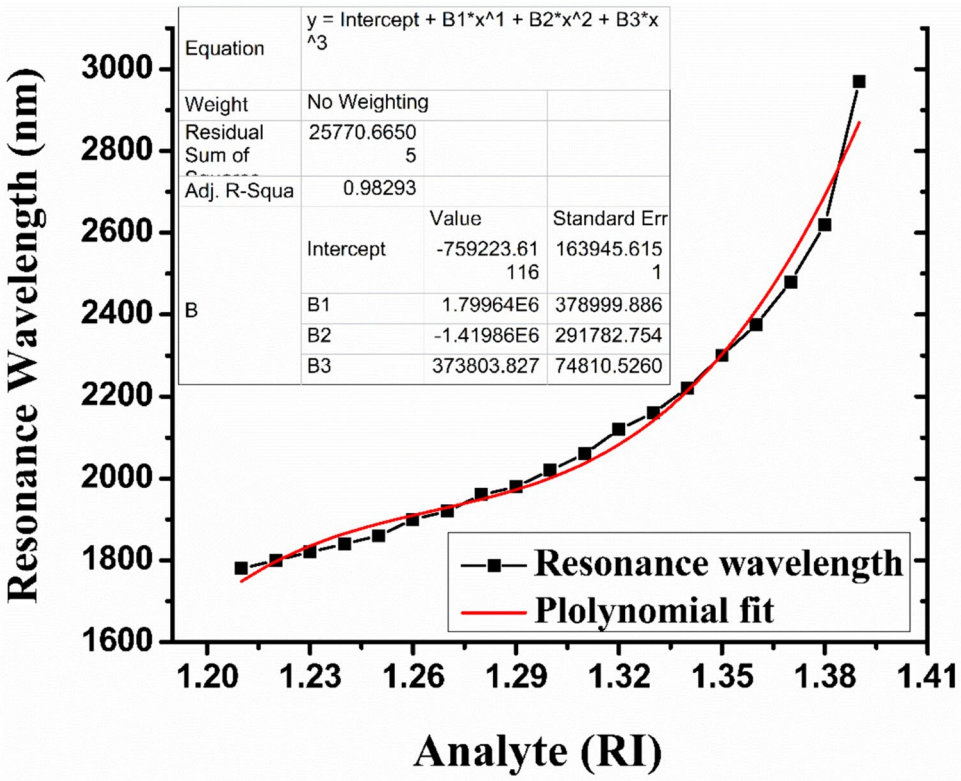

Conclusion

We have put forward the surface plasmon resonance phenomenon–based dual-core PCF sensor for detecting wide-range analyte RI of 1.21 to 1.39. The beauty of our simulation work of the proposed design is to reveal the sensing performance for long-range analyte RI. It provides a maximum wavelength sensitivity of 35,000 nm/RIU for analyte RI 1.38 to 1.39 and maximum amplitude sensitivity of 373 RIU^{-1}. The wavelength resolution is the order of 10^{-6} for analyte RI. The figure of merit is observed with the maximum value of 259 RIU^{-1}, which reveals the degree of performance of the proposed sensor. Regression analysis from polynomial curve fitting provides the maximum value of R^2 of 0.98293. Fabrication has become more accessible and fast due to the availability of recently developed technologies like the stack-and-draw method. From an application point of view, the proposed PCF sensor has the potential to work in different fields, such as biomedical and biochemical, for the detection of low refractive index range chemicals. The proposed PCF sensor may be utilized to reveal the stimulating application for pregnancy and alcohol tests.

Author Contribution All the authors have significant contribution in this paper.

Funding The authors received no specific funding for this work.

Data Availability Data and code of this work will be available from the corresponding author upon reasonable request.

Declarations

Competing Interests The authors declare no competing interests.

Conflict of Interest The authors declare no competing interests.

References

1. Homola J (2003) Present and future of surface plasmon resonance biosensors. Anal Bioanal Chem 377:528–539. https://doi.org/10.1007/s00216-003-2101-0
2. Fang S, Lee HJ, Wark AW, Corn RM (2006) Attomole microarray detection of microRNAs by nanoparticle-amplified SPR imaging measurements of surface polyadenylation reactions. J Am Chem Soc 128:14044–14046. https://doi.org/10.1021/ja065223p
3. Nooke A, Beck U, Hertwig A, Krause A, Krüger H, Lohse V, Negendank D, Steinbach J (2010) On the application of gold based SPR sensors for the detection of hazardous gases. Sensors Actuators, B Chem 149:194–198. https://doi.org/10.1016/j.snb.2010.05.061
4. Koubova V, Brynda E, Skvor L, Homola J, Dostalek J, P. Tobiska JR, (2001) Detection of foodborne pathogens using surface plasmon resonance biosensors. Sensors Actuators B 3:100–105
5. Sharma AK, Jha R, Gupta BD (2007) Fiber-optic sensors based on surface plasmon resonance: a comprehensive review. IEEE Sens J 7:1118–1129. https://doi.org/10.1109/JSEN.2007.897946
6. Robinson G (1995) The commercial development of planar optical biosensors. Sensors Actuators B Chem 29:31–36. https://doi.org/10.1016/0925-4005(95)01660-0
7. Jha R, Badenes G (2009) Effect of fiber core dopant concentration on the performance of surface plasmon resonance-based fiber optic sensor. Sensors Actuators, A Phys 150:212–217. https://doi.org/10.1016/j.sna.2009.01.004
8. Islam MS, Sultana J, Rifat AA et al (2018) Dual-polarized highly sensitive plasmonic sensor in the visible to near-IR spectrum. Opt Express 26:30347. https://doi.org/10.1364/oe.26.030347
9. Koshiba M (2004) Modeling of photonic crystal fibers. IEEJ Trans Fundam Mater 124:1088–1093. https://doi.org/10.1541/ieejfms.124.1088
10. Rifat AA, Amouzad Mahdiraji G, Chow DM et al (2015) Photonic crystal fiber-based surface plasmon resonance sensor with selective analyte channels and graphene-silver deposited core. Sensors (Switzerland) 15:11499–11510. https://doi.org/10.3390/s150511499
11. Hautakorpi M, Mattinen M, Ludvigsen H (2008) Surface-plasmon-resonance sensor based on suspended-core microstructured optical fiber. 2008 Jt Conf Opto-Electronics Commun Conf Aust Conf Opt Fibre Technol OECC/ACOFT 2008 16:2390–2392. https://doi.org/10.1109/OECCACOFT.2008.4610571
12. Dash JN, Jha R (2014) SPR biosensor based on polymer PCF coated with conducting metal oxide. IEEE Photonics Technol Lett 26:595–598. https://doi.org/10.1109/LPT.2014.2301153
13. Selvendran S, Susheel A, Tarun PV et al (2020) A novel surface plasmon based photonic crystal fiber sensor. Opt Quantum Electron 52:1–12. https://doi.org/10.1007/s11082-020-02403-8
14. Hasan MR, Akter S, Rifat AA et al (2018) Spiral photonic crystal fiber-based dual-polarized surface plasmon resonance biosensor. IEEE Sens J 18:133–140. https://doi.org/10.1109/JSEN.2017.2769720
15. Rifat A A, Mahdiraji G A, Ahmed R, et al (2016) Copper-graphene-based photonic crystal fiber plasmonic biosensor. IEEE Photonics J 8:. https://doi.org/10.1109/JPHOT.2015.2510632
16. Liu M, Yang X, Shum P, Yuan H (2018) High-sensitivity birefringent and single-layer coating photonic crystal fiber biosensor based on surface plasmon resonance. Appl Opt 57:1883. https://doi.org/10.1364/ao.57.001883
17. Paul KA, Md HS, Hai HN, Razzak AMS (2020) An air - core photonic crystal fiber based plasmonic sensor for high refractive index sensing. Opt Commun 464:125556. https://doi.org/10.1016/j.optcom.2020.125556
18. Haque E, Anwar Hossain M, Namihira Y, Ahmed F (2019) Microchannel-based plasmonic refractive index sensor for low refractive index detection. Appl Opt 58:1547. https://doi.org/10.1364/ao.58.001547
19. Malitson IH (1965) Interspecimen comparison of the refractive index of fused silica. J Opt Soc Am 55:1205. https://doi.org/10.1364/josa.55.001205
20. Mahfuz Al M, Afroj S, Rahman A et al (2024) Ultra-sensitive visible-IR range fiber based plasmonic sensor: a finite-element analysis and deep learning approach for RI prediction. IEEE Access 12:64727–64735. https://doi.org/10.1109/ACCESS.2024.3395390
21. Ramani U, Kumar H, Singh BK, Pandey PC (2020) Study of highly sensitivity metal wires assisted photonic crystal fiber based refractive index sensor. Opt Quantum Electron 52:1–13. https://doi.org/10.1007/s11082-020-02658-1
22. Liu Y, Gralak B, Guenneau S (2016) Finite element analysis of electromagnetic waves in two-dimensional transformed bianisotropic media. Opt Express 24:26479. https://doi.org/10.1364/oe.24.026479
23. Berenger JP (1994) A perfectly matched layer for the absorption of electromagnetic waves. J Comput Phys 114:185–200. https://doi.org/10.1006/jcph.1994.1159

24. Liu W, Hu C, Zhou L, Yi Z, Liu C, Lv J, Yang L, Chu PK (2020) Ultra-sensitive hexagonal PCF-SPR sensor with a broad detection range. J Mod Opt 67:1545–1554. https://doi.org/10.1080/09500340.2021.1872727
25. Liu W, Hu C, Zhou L et al (2022) A square-lattice D-shaped photonic crystal fiber sensor based on SPR to detect analytes with large refractive indexes. Phys E Low-dimensional Syst Nanostructures 138:115106. https://doi.org/10.1016/j.physe.2021.115106
26. Haque E, Mahmuda S, Hossain MdA, Hai NH, Namihira Y, Ahmed F (2020) Highly sensitive dual-core PCF based plasmonic refractive index sensor for low refractive index detection. Sensors 20:6049. https://doi.org/10.1109/JPHOT.2019.2931713
27. Ramani U, Kumar H, Kumar R et al (2023) Rectangular-shape cladding-based photonic crystal fiber surface plasmon resonance-based refractive index sensor. Plasmonics 18:921–929. https://doi.org/10.1007/s11468-023-01820-1
28. Haque E, Mahmuda S, Hossain MA et al (2019) Highly sensitive dual-core PCF based plasmonic refractive index sensor for low refractive index detection. IEEE Photonics J 11:1–9. https://doi.org/10.1109/JPHOT.2019.2931713
29. Al MM, Hossain MA, Haque E et al (2020) Dual-core photonic crystal fiber-based plasmonic RI sensor in the visible to near-IR operating band. IEEE Sens J 20:7692–7700. https://doi.org/10.1109/JSEN.2020.2980327
30. Yang Z, Xia L, Li C et al (2019) A surface plasmon resonance sensor based on concave-shaped photonic crystal fiber for low refractive index detection. Opt Commun 430:195–203. https://doi.org/10.1016/j.optcom.2018.08.049
31. Haider F, Aoni RA, Ahmed R, Miroshnichenko AE (2018) Highly amplitude-sensitive photonic-crystal-fiber-based plasmonic sensor. J Opt Soc Am B 35:2816. https://doi.org/10.1364/josab.35.002816
32. Jain S, Choudhary K, Kumar S (2022) Photonic crystal fiber-based SPR sensor for broad range of refractive index sensing applications. Opt Fiber Technol 73:103030. https://doi.org/10.1016/j.yofte.2022.103030
33. Sorathiya V, Lavadiya S, Faragallah OS, et al (2022) D shaped dual core photonics crystal based refractive index sensor using graphene–titanium–silver materials for infrared frequency spectrum. Opt Quantum Electron 54:0–13. https://doi.org/10.1007/s11082-022-03700-0
34. Islam N, Arif FH, M., Abu Yousuf, M. & , Asaduzzaman S, (2023) Highly sensitive open channel based PCF-SPR sensor for analyte refractive index sensing. Results Phys 46:106266. https://doi.org/10.1016/j.rinp.2023.106266
35. Melwin G, Senthilnathan K (2024) Modelling a simple arc shaped gold coated PCF-based SPR sensor. J Opt 53:117–126. https://doi.org/10.1007/s12596-023-01110-3
36. Sharif V, Pakarzadeh H (2023) High-performance surface plasmon resonance fiber sensor based on cylindrical vector modes. Sci Rep 13:4563. https://doi.org/10.1038/s41598-023-31524-9
37. Parvin T, Ahmed K, Alatwi AM, Rashed ANZ (2021) Differential optical absorption spectroscopy-based refractive index sensor for cancer cell detection. Opt Rev 28:134–143. https://doi.org/10.1007/s10043-021-00644-w
38. Belal SJ, Alameri LM, Rashid FF, Mansour TS (2019) Laser biosensor as for pregnancy test by using photonic crystal fiber. Institute of Laser for Postgraduate Studies, International Journal of Medical Research & Health Sciences 8:41–49
39. Arasu PT, Al-Qazwini Y, Onn BI, Noor ASM (2012) Fiber Bragg grating based surface plasmon resonance sensor utilizing FDTD for alcohol detection applications. ICP 2012 - 3rd Int Conf Photonics 2012, Proc 93–97. https://doi.org/10.1109/ICP.2012.6379852
40. Reeves W H, Ravi K K V V, George A K, J C Knight, Russell P S J, Omenetto F G, Efimov A, Taylor A J (2003) Broad supercontinuum generation from extruded soft glass photonic crystal fiber. In: Conference on Lasers and Electro-Optics/Quantum Electronics and Laser Science Conference, Technical Digest (Optica Publishing Group, 2003), paper CTuA3.
41. Nazirizadeh Y, von Oertzen F, Plewa K et al (2013) Sensitivity optimization of injection-molded photonic crystal slabs for biosensing applications. Opt Mater Express 3:556. https://doi.org/10.1364/ome.3.000556
42. Bise RT, Trevor DJ (2005) Sol-gel derived microstructured fiber: fabrication and characterization. Conf Opt Fiber Commun Tech Dig Ser 3:269–271. https://doi.org/10.1109/ofc.2005.192772
43. Pysz D, Kujawa I, Stepien R et al (2014) Stack and draw fabrication of soft glass microstructured fiber optics. Bull Polish Acad Sci Tech Sci 62:667–682. https://doi.org/10.2478/bpasts-2014-0073
44. Kamrunnahar QM, Mou JR, Momtaj M (2020) Dual-core gold coated photonic crystal fiber plasmonic sensor: design and analysis. Results Phys 18:103319. https://doi.org/10.1016/j.rinp.2020.103319
45. Chen X, Xia L, Li C (2018) Surface plasmon resonance sensor based on a novel D-shaped photonic crystal fiber for low refractive index detection. IEEE Photonics J 10:1–9. https://doi.org/10.1109/JPHOT.2018.2790424